HHS Public Access

Author manuscript

Biochemistry. Author manuscript; available in PMC 2022 April 27.

Published in final edited form as:

Biochemistry. 2021 April 27; 60(16): 1286–1298. doi:10.1021/acs.biochem.1c00165.

Probing the Diacylglycerol Binding Site of Presynaptic Munc13-1

Youngki You,
Department of Pharmacological & Pharmaceutical Sciences, College of Pharmacy, Health 2, University of Houston, Houston, Texas 77204, United States

Sachin Katti,
Department of Biochemistry and Biophysics, Texas A&M University, College Station, Texas 77843, United States

Binhan Yu,
Department of Biochemistry and Biophysics, Texas A&M University, College Station, Texas 77843, United States

Tatyana I. Igumenova,
Department of Biochemistry and Biophysics, Texas A&M University, College Station, Texas 77843, United States

Joydip Das
Department of Pharmacological & Pharmaceutical Sciences, College of Pharmacy, Health 2, University of Houston, Houston, Texas 77204, United States

Abstract

Munc13-1 is a presynaptic active zone protein that acts as a master regulator of synaptic vesicle priming and neurotransmitter release in the brain. It has been implicated in the pathophysiology of several neurodegenerative diseases. Diacylglycerol and phorbol ester activate Munc13-1 by binding to its C1 domain. The objective of this study is to identify the structural determinants of ligand binding activity of the Munc13-1 C1 domain. Molecular docking suggested that residues Trp-588, Ile-590, and Arg-592 of Munc13-1 are involved in ligand interactions. To elucidate the role of these three residues in ligand binding, we generated W588A, I590A, and R592A mutants in full-length Munc13-1, expressed them as GFP-tagged proteins in HT22 cells, and measured their ligand-induced membrane translocation by confocal microscopy and immunoblotting. The extent of 1,2-dioctanoyl-*sn*-glycerol (DOG)- and phorbol ester-induced membrane translocation decreased in the following order: wild type > I590A > W588A > R592A and wild type > W588A > I590A > R592A, respectively. To understand the effect of the mutations on ligand binding, we

Corresponding Authors: Joydip Das − Department of Pharmacological & Pharmaceutical Sciences, College of Pharmacy, Health 2, University of Houston, Houston, Texas 77204, United States; Phone: 713-743-1708; jdas@uh.edu; Fax: 713-743-1229; **Tatyana I. Igumenova** − Department of Biochemistry and Biophysics, Texas A&M University, College Station, Texas 77843, United States; tigumenova@tamu.edu.

Author Contributions

J.D. and Y.Y. designed the study. J.D., Y.Y., T.I.I., and S.K. analyzed the data and wrote the paper. Y.Y. performed protein purification, cell culture, confocal, and molecular modeling studies. S.K. and B.Y. performed NMR studies.

Accession Codes

Q62768 and P28867.

The authors declare no competing financial interest.

also measured the DOG binding affinity of the isolated wild-type C1 domain and its mutants in membrane-mimicking micelles using nuclear magnetic resonance methods. The DOG binding affinity decreased in the following order: wild type > I590A > R592A. No binding was detected for W588A with DOG in micelles. This study shows that Trp-588, Ile-590, and Arg-592 are essential determinants for the activity of Munc13-1 and the effects of the three residues on the activity are ligand-dependent. This study bears significance for the development of selective modulators of Munc13-1.

Graphical Abstract

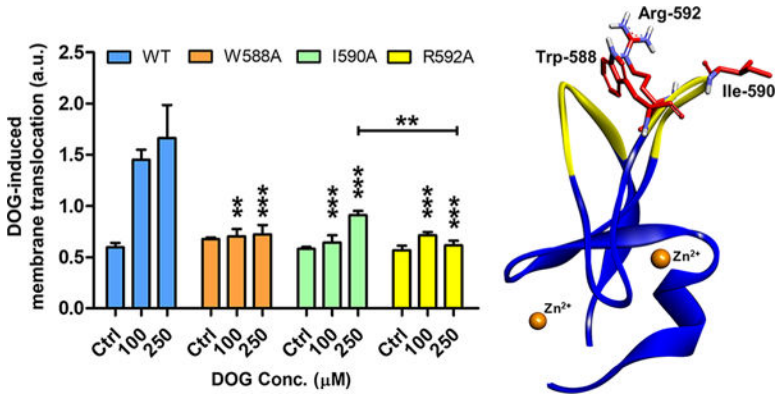

Munc13-1 is a presynaptic protein that regulates vesicle exocytosis by bridging the vesicle and the plasma membrane.[1–4] It facilitates the formation of the SNARE [soluble NSF (*N*-ethylmaleimide-sensitive factor) attachment protein receptor] complex by interacting with proteins, such as syntaxin-1 and Munc18, and regulating vesicle priming[5,6] and neurotransmitter release.[2,7] Multiple studies indicated Munc13-1's role in short-term presynaptic plasticity[8–13] and long-term potentiation.[14] Munc13-2, Munc13-3, and Munc13-4 are the other members of the Munc13 protein family.[15] Complete abolishment of neurotransmitter release was observed in the double-knockout mice of Munc13-1 and Munc13-2.[3,16–18] Munc13-1 has been implicated in the A_{β}-induced neurotoxicity in an Alzheimer' s disease model.[11,12,19,20] Clinical evidence suggested a strong correlation of single-nucleotide polymorphism in the Munc13-1 gene with amyotrophic lateral sclerosis and frontotemporal dementia.[21–24] Munc13-1's role has been implicated in neuron cells in amyotrophic lateral sclerosis[25] and motor neuron degeneration.[26] Additionally, Munc13-1 is involved in insulin release,[27] and recent studies highlighted the role of the Munc13 protein in alcoholism.[28–30]

Munc13-1 is an ~200 kDa protein consisting of three C2 domains (C2A, C2B, and C2C), one C1 domain, and a MUN domain. The C2A domain is at the N-terminus followed by the diacylglycerol (DAG)/phorbol ester binding C1 domain, the Ca^{2+} binding C2B domain, and the MUN domain, and the C2C domain is at the C-terminus.[17,31] The C2A domain forms a homodimer/heterodimer with the Rab3-interacting molecules (RIMs)[32–34] and regulates neurotransmitter release and Rab3- and RIM-dependent presynaptic plasticity.[35,36] The C2B domain binds to the plasma membrane and regulates Ca^{2+}- and PIP_2-dependent short-term plasticity.[37] The C1 domain binds to DAG/phorbol ester, and this binding lowers the

energy barrier for vesicle fusion and neurotransmitter release.[38,39] Phorbol ester binds to the C1 domain with an affinity higher than that of DAG.[40] The MUN domain is a rodlike module critical for opening syntaxin-1.[31,41,42] A recent study proposed a model in which Munc13-1 bridges the plasma membrane and synaptic vesicle membrane by binding the plasma membrane with its C1 and C2B domains and binding the vesicle membrane with its C2C domain while MUN acts as a tether between these domains.[43] There is a small region between the C2A and C1 domains, called the calmodulin-binging (CaMb) region, that is responsible for Ca^{2+}-dependent short-term plasticity.[44]

The C1 domain of Munc13-1 is structurally homologous to the C1 domain of protein kinase C (PKC). The phorbol 13- acetate-bound PKCδ C1B domain is the only ligand-bound C1 domain structure known to date.[45] Both PKCδ C1B [Protein Data Bank (PDB) entry 1PTR] and Munc13-1 C1 (PDB entry 1Y8F) have two membrane binding loops, two β-sheets, a short α-helix at the C-terminus, and two Zn^{2+} binding sites.[45,46] Although the ligand-bound structure of the Munc13-1 C1 domain is not known, on the basis of its structural similarity with PKCδ C1B, one would expect the DAG/phorbol ester to bind inside a groove between the two loops as seen in PKCδ C1B. A comparison of the residues of the ligand binding sites reveals that there are several differences in the residues and the orientation of their side chains. Leucine and lysine in PKCδ are replaced by isoleucine and arginine in Munc13-1 at homologous sites 590 and 592, respectively. The orientations of side chains of these residues are different in Munc13-1 and PKCδ (Figure 1). While in Munc13-1 the side chain of Trp-588 occludes the DAG/phorbol ester site, it does not do so in PKCδ. Mutation of this Trp-588 to other residues reduced its phorbol ester binding and phorbol ester-induced membrane translocation properties.[47] Homologous tryptophan in PKCδ C1B contributes to partitioning of the C1 domain into the membrane[48] and binding to DAG rather than phorbol ester.[49]

Binding of DAG/phorbol ester to C1 domains and subsequent activation of the protein depend on several factors, such as the lipophilicity of the ligand, the nature of the residues that interact with the ligand, the lipid composition, and other lipid-interacting domains.[50] In our previous study, we reported that the C1 domain of Munc13-1 with a net negative charge showed maximum phorbol ester binding at 20% phosphatidylserine (PS), unlike PKCδ C1B and PKCθ C1B with a net positive charge that showed maximum phorbol ester binding at 100% PS.[47,51]

In this study, we investigated the role of Trp-588, Ile-590, and Arg-592 in DAG- and phorbol ester-induced membrane translocation of Munc13-1 in HT22 cells using immunoblotting and confocal microscopy. Solution nuclear magnetic resonance (NMR) spectroscopy was used to monitor the interactions of the C1 domain with ligands in a residue-specific manner. Our results highlight the importance of Trp-588 in ligand-independent membrane partitioning and suggest electrostatic interactions as an additional important factor in the recognition of the membrane-embedded ligand.

MATERIALS AND METHODS

1,2-Dioctanoyl-*sn*-glycerol (DOG) and 2-dihexanoyl-*sn*-glycero-3-phospho-L-serine (DPS) were obtained from Avanti Polar Lipids (Alabaster, AL). Phorbol 12-myristate 13-acetate (PMA) was purchased from LC Laboratories (Woburn, MA). Phorbol-12,13-dibutyrate (PDBu) was obtained from Sigma-Aldrich (St. Louis, MO). Deuterated dodecylphosphocholine (d_{38}-DPC), DMSO (d_6-DPC), and $^{15}NH_4Cl$ were obtained from Cambridge Isotope Laboratories, Inc. (Tewksbury, MA). Protein quantification was conducted using the Bradford protein assay from Bio-Rad (Hercules, CA) and the BCA (bicinchoninic acid) protein assay kit from Thermo Fisher Scientific (Grand Island, NY). Glutathione sepharose 4B was obtained from GE Healthcare Life Sciences (Piscataway, NJ). HT22 cells were purchased from ATCC (Manassas, VA). Fetal bovine serum (FBS) was from ZenBio (Research Triangle Park, NC). *Rattus norvegicus* Munc13-1 conjugated with green fluorescent protein (GFP) was a generous gift from N. Brose (Max Planck Institute for Experimental Medicine, Gottingen, Germany). The rabbit anti-GFP antibody, rabbit anti-Na/K-ATPase antibody, rabbit anti-β-actin, and HRP (horseradish peroxidase)-conjugated rabbit anti-IgG antibody used for the Western blot analysis were obtained from Cell Signaling (Danvers, MA). All other reagents were purchased from either MilliporeSigma (Burlington, MA) or Thermo Fisher Scientific.

Site-Directed Mutagenesis of Full-Length Munc13-1 and the C1 Domain.

The W588A, I590A, and R592A single-point mutations in Munc13-1 (full-length) were generated by site-directed mutagenesis at Epoch Life Science (Sugar Land, TX) using the Munc13-1-pEGFP-N1 vector as the template. The corresponding mutations in the isolated C1 domain were introduced using the pGEX-2TK vector for expression as glutathione *S*-transferase (GST)-tagged proteins. The mutations were verified for their correct sequences using the sequencing facility at Epoch Life Science. The gene sequencing chromatograms of the mutants were analyzed using SnapGene Viewer (GSL Biotech LLC, San Diego, CA).

Cell Culture.

The HT22 hippocampal neuronal cell line was used for protein expression and membrane translocation studies. The HT22 cells were cultured in Dulbecco's modified Eagle's medium (DMEM) containing 10% FBS, L-glutamine (2 mM), streptomycin (100 μg/mL), and penicillin (100 units/mL) at 37 °C in a humidified atmosphere supplemented with 5% CO_2. Cells were plated on six-well plates for Western blotting (1.0×10^6 cells per well) or 12-well plates with 12 mm glass coverslips (VWE, Atlanta, GA) for confocal analysis (2.0×10^5 cells per well). Once they were 75−85% confluent, the cells were transfected with either pEGFPN1-Munc13-1WT, pEFGPN1-Munc13-1W588A, pEFGPN1-Munc13-1I590A, or pEFGPN1-Munc13-1R592A using Lipofectamine 3000 and P3000 reagent as per the manufacturer's instructions. The optimized ratio of the reagents was 1 μg of DNA to 1 μL of Lipofectamine 3000 to 1 μL of P3000 reagent. The growth medium deficient in antibiotics was used during transfection.

Cell Fractionation and Immunoblotting.

Proliferative HT22 cells expressing wild-type or mutant GFP-tagged Munc13-1 were treated with DOG (100 and 250 μM) for 15 min or PMA (1.0 and 5.0 μM) for 5 min. Subcellular fractionation was carried out using the subcellular fractionation kit (catalog no. 78840, Thermo Scientific Inc., Rockford, IL) following the manufacturer's recommendations. The kit extracts cytoplasmic and membrane fractions efficiently for the studies of the localization and distribution of proteins. Briefly, treated cells were lysed in cytosolic extraction buffer (CEB) for 10 min at 4 °C. The lysate in CEB was the cytosolic fraction. The cytosolic fraction was collected, and the cells were washed and harvested in ice-cold phosphate-buffered saline (PBS) and then centrifuged at 800*g* for 5 min. The pellet was mixed with membrane extraction buffer (MEB) and then incubated at 4 °C for 15 min. The sample in MEB was centrifuged at 3000*g* for 5 min, and the supernatant was collected as the membrane fraction. The concentration of proteins in each isolated fraction was measured by using the BCA kit, and 8 μg of protein was used for sodium dodecyl sulfate−polyacrylamide gel electrophoresis (SDS−PAGE) and Western blot analysis. The samples were prepared by mixing with a Laemmli sample buffer (LSB). The membrane fraction samples were prepared without heating. The dilutions of the antibody were as follows: 1:1000 anti-rabbit GFP, 1:1000 anti-rabbit Na,K-ATPase, and 1:2000 anti-rabbit β-actin (Cell Signaling). The protein bands were observed using the ChemiDoc Touch Imaging System (Bio-Rad) using the goat anti-rabbit HRP-linked secondary antibody. The bands were detected and acquired in the linear intensity range. The band intensity was quantitated using ImageLab 6.0.1 (Bio-Rad).

Confocal Microscopy.

HT22 cells were grown and transfected with the plasmid on 12 mm coverslips. After being treated with DOG (100 and 250 μM) or PMA (1.0 and 5.0 μM), the cells were washed with PBS and then fixed with 4% paraformaldehyde (PFA) for 10 min. The coverslips containing cells were mounted on microscope slides with mounting medium. The cells (GFP-tagged Munc13) were excited with an argon laser at 488 nm, and images were captured using a confocal microscope (100×, Leica SP8, Leica Microsystems). The distribution of Munc13-1 in the cytosol and the plasma membrane was quantified from confocal microscope images using ImageJ (http://rsb.info.nih.gov/ij/). The mean fluorescence intensities of the whole cell and plasma membrane of individual images were measured. The size of the plasma membrane was defined as 300 nm from the outer edge of the cell. The ratios of the mean intensity of the plasma membrane to the whole cells are presented as described previously.[52,53]

Expression and Purification of N^{15}-Labeled Munc13-1 C1 and Its Mutants for the NMR Study.

The pGEX-2TK vector (GE Healthcare Bio-Sciences, Pittsburgh, PA) was used to express the GST-conjugated C1 domain of Munc13-1. Munc13-1 C1 WT and its mutant, W588A, I590A, and R592A, plasmids were transformed into *Escherichia coli* BL-21(DE3) competent cells. The transformants were grown in LB medium at 37 °C for expression of the desired proteins until the optical density of the cell suspension reached 0.5−0.6. Isotope

labeling of Munc13-1 WT and its mutants was carried out by using the method of Marley et al.[54] Briefly, the cells grown on LB medium were resuspended and grown in M9 minimal medium, supplemented with 1 g/L $^{15}NH_4Cl$. Protein expression in M9 minimal medium was induced with 0.5 mM isopropyl β-D-1-thiogalactopyranoside (IPTG) and 10 μM $ZnSO_4$ at an optical density of 1.5−1.7, and the cells were grown at 15 °C for an additional 15−16 h. The cells were harvested and lysed in lysis buffer (PBS, 1 mg/mL lysozyme, and 0.1% Triton X-100) with sonication (15 times, 5 s, 30% amplitude) using a digital sonifier (model 250, Branson, Danbury, CT). Soluble protein was recovered by centrifugation at 7000*g* and 4 °C for 10 min, and the soluble extract was further treated with polyethylenimine (PEI) (0.1%) to remove nucleic acids. Extracted lysates were loaded onto a glutathione-sepharose column pre-equilibrated with PBS, and the column was washed with PBS until maximum amounts of impurity was eliminated. Protein was cleaved from its conjugated GST with thrombin on the column, and the protein was eluted in PBS. Eluted protein was further purified using a size exclusion column (Sephadex 75 10/300 GL, GE Life Science, Madison, CA) with gel filtration buffer [40 mM HEPES, 150 mM NaCl, and 50 μM $ZnCl_2$ (pH 7.0)]. The purity of the protein was examined by SDS−PAGE analysis followed by Coomassie staining (Instant Blue, Expedeon, San Diego, CA).

NMR Sample Preparation.

After purification, Munc13-1 C1 and its variants were concentrated and exchanged into an "NMR buffer" containing 40 mM HEPES (pH 7.0), 150 mM NaCl, 50 μM $ZnCl_2$, and 8% D_2O. A stock solution of mixed micelles was prepared by combining chloroform solutions of DPS and d_{38}-DPC at a molar ratio of 3:7. Chloroform was removed under a mild stream of nitrogen gas followed by 2 h under vacuum. The DPS/DPC detergent film was resuspended in NMR buffer and vortexed for 1 min to form a clear micellar solution. Stock solutions of DOG and PDBu were prepared in d_6-DMSO. The concentration of DMSO at the titration end point was <8% (v/v).

NMR Spectroscopy.

The NMR experiments were carried out at 25 °C on either an 11.7 T AVANCE III HD or a 14.1 T (both AVANCE III HD and NEO) NMR instrument equipped with room-temperature (11.7 T) and cryogenically cooled (14.1 T) probes. The temperature was calibrated with methanol. The NMR-detected binding experiments were carried out by adding stock solutions of micelles to 100 μM [U-^{15}N]C1 or stock solutions of an agonist (DOG or PDBu) to the mixture of 100 μM [U-^{15}N]C1 and 20 mM DPS/DPC micelles. The binding was monitored as a change in protein cross-peak position in a series of two-dimensional $^{15}N-^{1}H$ HSQC/SOFAST-HMQC spectra at different ligand concentrations. All NMR spectra were processed with NMRPipe[55] and analyzed with SPARKY (https://www.cgl.ucsf.edu/home/sparky/). Residue-specific binding curves were constructed by plotting the combined chemical shift perturbation $\Delta\delta = \sqrt{\Delta\delta_H{}^2 + (0.152\Delta\delta_N)^2}$ as a function of total ligand concentration L_0. The apparent dissociation constant (K_d) was determined by fitting the binding curves globally to the single-site binding equation:[56]

$$\Delta\delta = \Delta\delta_{max}\left\{K_d + P_0 + L_0 - \left[(K_d + P_0 + L_0)^2 - 4P_0L_0\right]^{1/2}\right\}/2P_0$$

where $\Delta\delta_H$ and $\Delta\delta_N$ are the chemical shift changes of the ^1H and ^{15}N nuclei, respectively, $\Delta\delta_{max}$ is the maximum chemical shift change upon saturation, and P_0 is the total concentration of C1.

Molecular Docking.

Phorbol 13-acetate was docked into the WT C1 domain of Munc13-1 using AUTODOCK 4.2. The molecular docking was prepared, run, and analyzed using AutoDockTools (ADT). The structure of phorbol 13-acetate was prepared using ChemBioDraw version 12.0, and then energy minimization was performed for the ligand with a 0.1 root-mean-square kcal mol^{-1} $Å^{-2}$ gradient level using MOE 2018 (MOE, Chemical Computing Group, Montreal, QC). The NMR structure of the Munc13-1 C1 domain (PDB entey 1Y8F) was used for the molecular docking.[46] Gasteiger charges and Kollman charges were given to the ligand and the proteins, respectively. For the docking space of the ligand, a grid box was generated and centered on the geometry of the phorbol 13-acetate in phorbol 13-acetate-bound PKCδ C1B (PDB entry 1PTR), which is the homologue of Munc13-1 C1.[45] The grid box included the residues of the active site between the two loops of C1 within a box size set at x = 40 Å, y = 55 Å, and z = 40 Å. The best 20 conformers were determined using the Lamarckian genetic algorithm (LGA) during the molecular docking. The volume of the binding pocket of PKCδ C1B and Munc13-1 C1 was measured using MOE. The phorbol 13-acetate-docked structures were visualized using Discovery Studio Visualizer 4.5 (DS, Biovia Inc., San Diego, CA).

Statistical Analysis.

Statistical analysis of data was conducted using Prism 5.0 software (GraphPad Software, Inc., San Diego, CA). At least three independent experiments were used for all of the statistical analysis. Raw data from DOG and PMA treatments of HT22 cells were first analyzed using two-way analysis of variance (ANOVA), and then Bonferroni's multiple-comparison post hoc tests were performed to compare all treatment groups. Differences at the $P < 0.05$ level were considered significant.

RESULTS

The Ligand Binding Site of Munc13-1 C1 Is Different from That of PKCδ C1B.

Munc13-1's presynaptic function is dependent on its activation by DAG, which binds to its C1 domain. Although the structure of Munc13-1 C1 has been elucidated,[46,57] the activator-bound structure is not known at present. To identify the residues of the C1 domain in activator binding, we used the activator-bound structure of PKCδ C1B (PDB entry 1PTR), a structural homologue of Munc13-1 C1, as a template. A comparison of the sequence and structures of ligand binding sites of the Munc13-1 C1 domain (PDB entry 1Y8F) and PKCδ C1B (PDB entry 1PTR) suggests that there are several differences in the residues and the

orientation of their side chains. This includes residues Trp-588, Ile-590, and Arg-592 (Figure 1B) and the orientation of their side chains (Figure 2).

Molecular docking results suggest phorbol 13-acetate docked into the active site of Munc13-1 between the two loops and Trp-588, Ile-590, and Arg-592 form the phorbol ester binding site (Figure 2A). The phorbol ester formed three hydrogen bonds, one each with Trp-588, Ile-590, and Arg-592. The docking site is similar to those of our previous docking studies for resveratrol and bryostatin-1.[58,59] However, in PKCδ C1B, the phorbol 13-acetate formed three hydrogen bonds with Thr-242 and Leu-251 that are located deep inside the binding pocket (Figure 2B). The phorbol 13-acetate binding sites of Munc13-1 C1 and PKCδ C1B (PDB entry 1PTQ) are slightly different because of the different orientation of Trp-588. While Trp-588 of Munc13-1 is oriented between the two loops, in PKCδ C1B the homologous Trp-252 resides outside of the two loops. This particular orientation of Trp-588 formed an alternative shallow pocket in Munc13-1 C1 instead of a deep pocket present in PKCδ C1B (Figure 2 and Figure S1). Indeed, the phorbol 13-acetate could adhere closely to PKCδ C1B rather than to Munc13-1 C1. This is because PKCδ C1B has a pocket volume of 88.4 Å^3, while the volume of the pocket in Munc13-1 C1 is 33.4 Å^3 (Figure S1). The pocket surface area of PKCδ C1B (111.3 Å^2) is also ~2 times larger than that of Munc13-1 C1 (50.3 Å^2). The ligand binding pocket of Munc13-1 C1 is surrounded by Trp-588, Ile-590, and Arg-592 (Figure 2A). To understand the role of these residues in the activity and ligand binding, we generated I590A, R592A, and W588A mutants in full-length Munc13-1 and in the isolated C1 domain. For the full-length protein, we performed functional assays using immunoblotting and confocal microscopy, and for the isolated C1 domain, we conducted NMR-detected binding studies.

Effect of Mutations of Trp-588, Ile-590, and Arg-592 on the Membrane Translocation of Full-Length Munc13-1.

On the basis of our docking results, we identified three residues, Trp-588, Ile-590, and Arg-592, in the C1 domain of Munc13-1 that could potentially interact with the ligand. To understand the role of these three residues in ligand-induced membrane translocation, three mutants, W588A, I590A, and R592A, were generated and expressed as GFP-conjugated full-length Munc13-1 in HT22 cells. The cells were treated with either DOG for 15 min or PMA for 5 min and imaged by confocal microscopy (Figure 3). DOG induced the translocation of wild-type Munc13-1 from the cytosol to the plasma membrane (Figure 3A). However, the extent of translocation of the mutants was significantly lower than that of wild-type Munc13-1 at both 100 and 250 μM doses. The extent of translocation decreases in the following order: WT > I590A > W588A > R592A. The difference between W588A and R592A was not significant. PMA also induced the translocation of wild-type Munc13-1 to the plasma membrane (Figure 3B). The 1.0 and 5.0 μM PMA treatment groups showed 5 and 7 times more translocation, respectively, than the no treatment group. The extent of translocation decreases in the following order for either PMA concentration: WT > W588A > I590A > R592A. The order of translocation for the wild type and the mutants, however, was slightly different than what was found for DOG. The reduced level of translocation of W588A compared to that of the wild type is similar to the result using living cell images reported in our previous study.[47] For the wild type, there was a difference in translocation

at two different concentrations of PMA, but this difference was not prominent for the mutants. For the mutants, there were significant differences in translocation between the PMA treatment and control groups, but there was not much difference in the mutants between the DOG treatment and control groups.

The relative membrane translocation of the wild type and the mutants was also analyzed by cell fractionation and immunoblotting. Like the confocal analysis results, the results of immunoblotting analysis also showed a decrease in the extent of translocation of mutants compared to that of wild-type Munc13-1 for either DOG or PMA (Figure 4). For DOG, the mutants showed significantly less translocation at both 100 and 250 μM compared to the wild type (Figure 4A). At 250 μM, the extents of translocation of W588A, I590A, and R592A were 43%, 57%, and 39% of that of the wild type, respectively. The extent of translocation decreased in the following order: WT > I590A > W588A > R592A. This order is similar to the order obtained in the confocal analysis for DOG treatment groups. At 5.0 μM PMA, the translocation levels of W588A, I590A, and R592A were 61%, 40%, and 43% of that of the wild type, respectively. Overall, the extent of translocation decreases in the following order: WT > W588A > I590A > R592A. This order of translocation is different than the order found in the case of the DOG treatment group but follows the same order as determined with the confocal analysis of the PMA treatment group. Only at 1.0 μM was there no significant difference in the extent of translocation between W588A and WT.

In summary, both DOG and PMA induced translocation of Munc13-1 from the cytosol to the plasma membrane and PMA was more potent than DOG. Mutation of Trp-588, Ile-590, and Arg-592 to alanine caused a decrease in the extent of translocation, and the extent of this reduction was dependent on the ligand.

Munc13-1 C1 Partitions into a Hydrophobic Environment in a Ligand-Independent Manner.

The translocation studies described above were conducted with full-length Munc13-1 in a cellular context. We used solution NMR spectroscopy of the isolated C1 domain to gain residue-specific insights into the activator−protein interactions.

We first sought to evaluate the propensity of the Munc13-1 C1 domain to partition into a hydrophobic environment in a ligand-independent manner. This experiment mimics a scenario in which C1 is initially recruited to the membranes but is not yet ligand-bound. The binding of the U-^{15}N-enriched Munc13-1 C1 domain to DPC/DPS (70:30) mixed micelles was characterized by two-dimensional (2D) solution NMR spectroscopy. The suitability of mixed micelles as a membrane mimic and successful application of NMR spectroscopy to probe C1 interactions have been demonstrated by us previously for the C1B domains of PKCα and PKCδ.[48,60] The partitioning of C1 domains from the aqueous state into a hydrophobic environment causes chemical shift perturbations (CSPs) of the amide (NH) cross-peaks in the 2D ^{15}N−^{1}H HSQC spectra. This provides us with the means to conduct residue-specific analysis of these interactions. The binding of the Munc13-1 C1 domain to micelles falls into the “fast” exchange regime on the NMR chemical shift time scale (Figure 5A). The binding curves were constructed by plotting the CSP values as a function of detergent concentration. The data were fitted with the single-site binding equation to obtain an apparent dissociation constant (K_d) of 104 μM (Figure 5B). These results indicate that the

Munc13-1 C1 domain possesses a high degree of amphiphilicity and can partition into the hydrophobic environment in a ligand-independent manner. The residues that experienced the most chemical shift perturbations belong to the loop regions that form the binding groove (Figure 6A).

Munc13-1 C1 Binds Endogenous Activator DAG and Tumor-Promoting Phorbol Ester PDBu.

The next step was to characterize the interactions of the C1 domain with diacylglycerol. The NMR structural ensemble of the Munc13-1 C1 domain (PDB entry 1Y8F) determined by Rizo's laboratory shows that the binding groove is occluded by the Trp-588 side chain.[46] This led to the hypothesis that considerable conformational rearrangement (necessary to remove the occlusion) would decrease the affinity of C1 for diacylglycerol.[46] To quantify the diacylglycerol affinity, we conducted NMR-detected DOG binding experiments in the presence of DPC/DPS (70:30) micelles. The binding of DOG to C1 was in the fast-to-intermediate exchange regime (Figure 5C). Nearly all loop residues were in the intermediate regime and hence broadened beyond detection (Figure 6B). The CSPs of the fast-exchanging residues were used to construct the binding curves, whose analysis produced an apparent dissociation constant of 118 μM for the C1−DOG interactions (Figure 5D). This affinity is ~600-fold weaker than that of PKCδ C1B that was measured under similar experimental conditions.[48] The low affinity of the Munc13-1 C1 domain for diacylglycerol supports the Trp-588 occlusion model proposed by Rizo's group.[46]

Diacylglycerol is a weaker C1 ligand compared to non-endogenous phorbol ester PDBu, a known tumor-promoting agent. To determine how the W588 occlusion influences C1−PDBu interactions, we first added a stoichiometric amount of PDBu to U-^{15}N-enriched Munc13-1 C1 in the presence of 20 mM DPC/DPS (70:30) mixed micelles. Large CSPs were observed in the spectra for many cross-peaks (Figure 7). Addition of PDBu to a 1:2 ratio did not cause any further perturbations in the spectra, suggesting that the formation of the high-affinity C1−PDBu complex takes place at stoichiometric protein and ligand concentrations. This is also consistent with the notion that the Munc13-1 C1 domain is a cellular target for high-affinity phorbol ester binding.[40] The stoichiometric binding of PDBu to C1 precludes the assignment of resonance identities in the PDBu-bound state based on the 2D spectra. However, we were able to identify several residues of the loop region that were perturbed significantly (Figure 7A, Trp-572/588, Thr-576, and Gly-585). The effect of PDBu binding was particularly prominent for the Nε−Hε resonance of the Trp-588 side chain (Figure 7B). In addition, two residues that reside on the α-helical region of the domain, His-605 and Glu-606, showed significant perturbations. Overall, the CSP data show a major change in the electronic environment of the ligand binding loops and Trp-588 side chain. These findings are consistent with Rizo's model[46] that involves a conformational change due to the displacement of the Trp-588 side chain from the binding groove.

Factors That Influence Munc13-1 C1−Diacylglycerol Recognition.

It is proposed that Munc13 exists in the autoinhibited state akin to the DAG-sensitive PKC isoforms.[38,61] Both C1 and C2B domains play a role in the inhibition of synaptic transmission by Munc13.[61] Interactions of C1 with the membrane-embedded DAG are

believed to facilitate the release of such an inhibitory state. Therefore, understanding how the Munc13-1 C1 ligand binding region partitions into the hydrophobic environment, where it recognizes and captures its ligands, is essential. At the atomistic level, this process could be driven by two types of conserved C1 residues[45,62,63] that have (1) aromatic and hydrophobic side chains that engage in the interactions with apolar lipid moieties and (2) charged side chains that guide the domain to anionic lipid headgroups. These factors were investigated sequentially with NMR using three Munc13-C1 variants: W588A, I590A, and R592A.

The W588A 2D $^{15}N-^{1}H$ SOFAST-HMQC spectrum revealed significant perturbations of the loop residues compared with the spectrum of the wild-type Munc13-1 C1 domain (WTC1) (Figure 8A). This is expected due to the occluding orientation of the Trp-588 side chain in the apo state, and the contacts made with the other loop residues: Ala-574, Thr-575, Thr-576, and Arg-592. The perturbation of Glu-606, a residue at the hinge of the helix away from the loops, suggests that the W588A mutation may have an allosteric effect on the other regions of the domain. The overall chemical shift dispersion of the W588A resonances indicates that the mutation does not affect the domain fold.

The tryptophan residue at the analogous position of the PKCδ C1B domain (Trp-252) is essential for the high-affinity PKCδ−DAG interactions[48,49,64] and has been described as the “DAG toggle”. In Munc13-1 C1, Trp-588 is also essential for DAG binding.[46] To dissect the specific role of Trp-588 in membrane partitioning and DAG recognition steps, we conducted NMR-detected micelle and DOG binding experiments. In sharp contrast to WTC1, addition of DPC/DPS mixed micelles to the W588A variant caused no detectable CSPs (Figures 8B and 5C), indicating that the mutation abrogates the C1−micelle interactions. Inclusion of DOG in the micelles produced only minor perturbations indicating negligible binding (Figure 8B). We conclude that the extremely low affinity of W588A for DAG, observed in CHAPS[46] and in our membrane-mimicking system, is due to the inability of this variant to partition into the hydrophobic environment. As a result, membrane-embedded DAG becomes inaccessible to the protein and no productive protein−ligand complex is formed. Our NMR data clearly establish the pivotal role of Trp-588 in the membrane recruitment of the Munc13-1 C1 domain.

Next, we acquired the 2D $^{15}N-^{1}H$ SOFAST-HMQC spectra of the I590A and R592A variants and compared them with that of WTC1 (Figure S2). A large chemical shift dispersion of resonances for both variants indicates the preservation of the three-dimensional fold (Figure S2A,B). The extent of CSPs was less prominent for these mutants than for W588A, allowing a reliable transfer of resonance assignments from WTC1. The CSP analysis using WTC1 as a reference shows that both mutations perturb the loop regions (Figure S2C,D). The nature of these perturbations could be structural and/or dynamical in origin. In the I590A variant, the side chain of Trp-588, which belongs to loop 2, is relatively unperturbed. However, the backbone N−H resonances of the loop 2 region show significant perturbations. The isoleucine to alanine mutation preserves the hydrophobic nature of the side chain, and the Ile-590 side chain does not appear to interact with any residues in the NMR ensemble of WTC1. It is therefore possible that small changes in the hydrophobicity

of this region have allosteric effects on the overall interaction network of the loops. Further studies are needed to explore these possibilities.

In the R592A variant, the side chain Nε−Hε resonance of Trp-588 is broadened beyond detection. Given the proximity of the Arg-592 side chain to the indole ring of Trp-588 in the NMR ensemble (Figure S2, inset),[46] it is plausible that they can be engaged in cation−π interaction. The disruption of this interaction due to alanine mutation could alter the loop dynamics and thereby result in the broadening of the Trp-588 Nε–Hε resonance.

We tested the effect of these mutations on interactions of C1 with micelles and DOG (Figure 9). Unlike W588A, both I590A and R592A variants partition readily into the DPC/DPS (70:30) mixed micelles as reported by the CSPs (Figure 9A,C). Changes induced by the additions of DOG were monitored by collecting a series of 2D ^{15}N−^{1}H SOFAST-HMQC spectra at each concentration point. Similar to WTC1, the loop resonances showed chemical shift changes (Figure 9A,C) in the intermediate-to-fast exchange regime for both variants. Plotting these changes as a function of DOG concentration (Figure 9B,D) produced apparent dissociation constants of 200 μM (I590A) and 390 μM (R592A). Compared to that of WTC1, these affinities are ~1.5-fold (I590A) and 3-fold (R592A) weaker. Because the Ile to Ala mutation preserves the hydrophobic nature of the position, the effect on DOG binding is expectedly smaller. In contrast, the R592A mutation neutralizes the positive charge, while concomitantly increasing the hydrophobicity of the loop region. A more significant effect of the R592A mutation on the DOG affinity suggests that electrostatics may substantially contribute to the formation of the ternary Munc13-1 C1−ligand−membrane complex.

Taken together, our experiments with Munc13-1 C1 mutants establish the significance of Trp-588 in ligand-independent membrane partitioning and suggest electrostatic interactions as an additional important factor in the recognition of the membrane-embedded ligand. Because membrane partitioning and ligand recognition in the C1 domains are influenced by the concerted actions of multiple residues, loop region dynamics may also play an important role in the mechanism of DAG sensing.

DISCUSSION

Munc13-1 acts as a master regulator of neurotransmitter release machinery in the brain[7,14,65] and has been implicated in the pathophysiology of Alzheimer's disease[66,67] and alcohol addiction.[28,30] Knowledge of the activator binding site of Munc13-1 is expected to aid in developing Munc13-1 modulators for intervening in these disease states. Toward this end, we identified the core residues in the activator binding site of the Munc13-1 C1 domain and characterized their contribution to Munc13-1 activation and interactions with ligands using ligand-induced membrane translocation assays and NMR-detected binding experiments, respectively. Using molecular docking, we first identified Trp-588, Ile-590, and Arg-592 as potential ligand-interacting residues (Figure 2). To understand the role of these residues in the activity of Munc13-1, we generated the corresponding alanine mutants and measured their ligand-induced membrane translocation. The efficiency of DOG-induced membrane translocation decreased in the following order: WT > I590A > W588A > R592A. The efficiency of PMA-induced membrane translocation decreased in the following order: WT >

W588A > I590A > R592A. This suggests that the translocation is dependent on the type of ligand.

In the isolated C1 domain, the apparent binding affinity of DOG for the purified C1 domain wild type and mutants in the DPS/DPC micelles decreased in the following order: WT > I590A > R592A (Figures 5 and 6). We did not detect any binding of W588A either with micelles or with DOG in the presence of micelles. This suggests that Trp-588 plays a more critical role in the binding of Munc13-1 C1 to the lipid membrane than that of Ile-590 and Arg-592. Trp-588 is known play a role in the interaction between the C1 domain and membrane through its hydrophobic side chain.[47] Tryptophan can potentially engage in several types of interactions, such as cation−π bonds between its fused aromatic ring system and positively charged choline groups of the lipids and detergents,[68] hydrogen bonds, N−H…π bonds, π-stacking, and C−H···π bonds.[69] Substitution of Trp with Ala in W588A is expected to show weakened or no DOG binding.

As the most hydrophobic residue of the rim of the two loops in Munc13-1 C1, Ile-590 may also play a role in the hydrophobic interaction between the C1 domain and membrane (Figures S3 and S4). Thus, the DOG binding affinity of I590A was decreased 1.7-fold compared to the affinity in the wild type (Figures 5D and 9B). However, I590A showed a higher affinity for DOG than either W588A or R592A, because isoleucine and alanine do not differ significantly in chemical composition, polarity, or molecular volume according to Grantham's distance.[70] The physico-chemical distances (calculated using the chemical composition, polarity, and molecular volume in an equation) between Ile and Ala, Trp and Ala, and Arg and Ala are 94, 148, and 112, respectively, suggesting that the Ile to Ala substitution will have a weaker influence on binding and/or activity as compared to Trp to Ala or Arg to Ala substitution.

Among the residues in the DOG binding site, Arg-592 is the most hydrophilic residue, and our NMR titration (Figures 6 and 9) and modeling (Figure S4 showing how arginine can be embedded into the lipid headgroup region in the membrane) results suggest that Arg-592 interacts with the lipid membrane and ligand. The guanidinium group of arginine can form multiple hydrogen bonds with the polar group of the lipid head and also can be located in the membrane at the depth of the hydrocarbon core with its hydrophobic aliphatic hydrocarbon chain.[71] These properties of arginine may explain why it can penetrate into the lipid membrane.[72] The positive charge of Arg-592 was neutralized in R592A, and therefore, its affinity for DOG in micelles was lower than those of the wild type and I590A (Figures 3, 4, and 9). Also in the membrane translocation assay, R592A showed the lowest activity because Arg-592 could strongly interact with the negatively charged phosphatidylserine in the cellular context, but Ala-592 could not. These results highlight the importance of electrostatic interactions in the ternary complex (Munc13-1 C1−ligand−lipid membrane) and the function of Mun13-1 as reported previously.[47]

The crystal structure of PKCδ C1B complexed with phorbol 13-acetate is the only ligand-bound C1 domain structure known to date.[45] How different is the Munc13-1 activator binding site compared to PKCδ? In PKCδ C1B, several hydrophobic residues lining the two activator binding loops facilitate its binding to the plasma membrane.[48,60,73] Once the

phorbol ester or DAG binds to the rim of the two loops, it covers the hydrophilic region and enhances the interaction between the C1 domain and the plasma membrane.[48,73] It was found previously that PKCδ C1B did partition into the DPS/DPC micellar system with a K_d value of 9 μM in the absence of any ligand.[48] In the study presented here, Munc13-1 C1 bound to the lipid micelles and partitioned into the micelles with a K_d value of 104 μM in the absence of any ligand (Figure 5A,B). This ~10-fold higher value of K_d for Munc13-1 could be due to the presence of fewer hydrophobic residues on the rim of two loops as compared to that in PKCδ C1B, judging the amino acid properties by the Kyte−Doolittle hydrophobicity scale (Figure S3).[74] In PKCδ C1B, Met-239 forms a hydrophobic surface, but the homologous residue of Munc13-1 C1 (Thr-575) forms a hydrophilic surface. Moreover, the Trp-588 residing inside the two loops causes a decrease in the hydrophobic surface area of the rim of the two loops. Furthermore, the positively charged Arg-592 of Munc13-1 C1 is exposed to the plasma membrane unlike the homologous Lys-256 of PKCδ C1B, which is oriented away from the membrane. The apparent K_d of DOG with respect to Munc13-1 C1 (118 μM) is ~600-fold weaker than that of PKCδ C1B (<0.2 μM).[48] Collectively, these data suggest that differences in both ligand-independent membrane partitioning and intrinsic DOG affinities contribute to the differential DOG responses of Munc13-1 and PKCδ.

Another major difference between Munc13-1 C1 and PKCδ C1B is the orientation of Trp-588. In Munc13-1, Trp-588 occludes the ligand binding site as evidenced by both the solution[46] and the crystal structure,[57] while in PKCδ C1B, the homologous Trp-252 resides outside the ligand binding loop. The Rizo group suggested[46] that this particular orientation could be the reason why Munc13-1 C1 has a lower affinity for DOG compared to that of PKCδ C1B. Now, does Trp-588 change its orientation when the ligand binds to Munc13-1 C1? A structural analysis of the solution structure of Munc13-1 (PDB entry 1Y8F) suggests that there are amide-π stacked hydrophobic interactions between Trp-588 and Thr-576 and π-alkyl hydrophobic interactions between Trp-588 and Pro-577, between Trp-588 and Ala-574, and between Trp-588 and Arg-592 (Figure S5). A molecular dynamics simulation (80 ns) of Munc13-1 C1 in the absence of a ligand and the membrane showed minimal movement of Trp-588, unlike the homologous tryptophan in PKCδ C1B that undergoes substantial rotameric flips.[47] In the C1B domains of PKCα and PKCδ, the loop regions are highly dynamic as revealed by the NMR studies.[60,75] The lack of Trp-588 displacement in the MD data might indicate that the dynamics of the Munc13-1 C1 loop region is on a slower time scale. The docked C1−phorbol 13-acetate complex may therefore represent initial interaction of the C1 domain with the ligand. A rotation of Trp-588 out of the loop region likely follows, allowing full accommodation of the ligand in the binding groove. Large chemical shift perturbations of the Nε−Hε resonance observed in the NMR spectra of the PDBu-complexed C1 domain, and the intermediate exchange regime of the Nε−Hε resonance in the DOG-complexed spectra (Figure 7B), suggest that significant changes in the electronic environment of the Trp side chain take place as a result of ligand interactions. This is consistent with the Trp side chain movement upon ligand binding.

The exact orientation of the Trp side chain in the complex may also depend on the chemical identity of the ligand. The C1 domain-interacting moiety of phorbol esters is ~3 times larger than that of DOG (excluding the amphiphilic chains that interact with hydrophobic

lipid tails of the plasma membrane) and contains four rings that are conformationally restrained. The number of potential hydrogen bond donors and acceptors is also different for the two ligands. The differences in the protein−ligand van der Waals interactions and hydrogen-bonding patterns may therefore dictate the Trp side chain orientation and underlie the functional response (Figures 3 and 4). High-resolution structures of agonist-bound Munc13-1 C1 domain complexes are required to determine the extent of the binding site arrangement that takes place in the C1 domain of Munc13-1. If such information is obtained, the distinctive structural features of the Munc13-1 activator binding site could be exploited in designing a selective modulator of Munc13-1, one of the 70 different C1 domain-containing proteins.

Our results showing that the DOG-induced activity of the full-length Munc13-1 mutants, particularly W588A, does not exactly correlate with the binding affinity of the isolated C1 domain suggest that domain−domain interaction may play a role in the DOG-induced activity of Munc13-1. A recent structure of the C1, C2B, and MUN domains of Munc13-1 (PDB entry 5UE8) revealed that the C1 and C2B domains are in the proximity of each other and the surface residues, Tyr-581, Glu-582, and Glu-584, of the C1 domain interact with the surface residues, Gln-717, Arg-750, Lys-752, and Arg-754, of the C2B domain through hydrogen bonds and electrostatic interactions. The C2B domain also binds to the plasma membrane following Ca^{2+} binding.[76] Therefore, Ca^{2+}-bound C2B could influence the C1−ligand−plasma membrane interactions in the full-length protein, but not in the isolated C1 domain.

In summary, our study characterized Trp-588, Ile-590, and Arg-592 as the ligand binding residues of Munc13-1 and found that DAG and phorbol ester could interact differently with these residues. Further time-resolved structural studies are required to understand the relative orientation of these residues in the membrane in the presence of various ligands.

Supplementary Material

Refer to Web version on PubMed Central for supplementary material.

ACKNOWLEDGMENTS

The authors thank Dr. N. Brose of the Max Planck Institute for Experimental Medicine (Göttingen, Germany) for providing us with the constructs for Munc13-1.

Funding

This research has been supported in part by funding from National Institutes of Health Grants 1R01AA022414 (J.D.) and R01 GM108998 (T.I.I.), National Science Foundation Grant CHE-1905116 (T.I.I.), and Welch Foundation Grant A-1784 (T.I.I.).

REFERENCES

(1). Rodarte EM, Ramos MA, Davalos AJ, Moreira DC, Moreno DS, Cardenas EI, Rodarte AI, Petrova Y, Molina S, Rendon LE, Sanchez E, Breaux K, Tortoriello A, Manllo J, Gonzalez EA, Tuvim MJ, Dickey BF, Burns AR, Heidelberger R, and Adachi R (2018) Munc13 proteins control regulated exocytosis in mast cells. J. Biol. Chem 293, 345–358. [PubMed: 29141910]

(2). Betz A, Ashery U, Rickmann M, Augustin I, Neher E, Sudhof TC, Rettig J, and Brose N (1998) Munc13−1 is a presynaptic phorbol ester receptor that enhances neurotransmitter release. Neuron 21, 123–136. [PubMed: 9697857]

(3). Augustin I, Rosenmund C, Sudhof TC, and Brose N (1999) Munc13−1 is essential for fusion competence of glutamatergic synaptic vesicles. Nature 400, 457–461. [PubMed: 10440375]

(4). Rizo J (2018) Mechanism of neurotransmitter release coming into focus. Protein Sci 27, 1364–1391. [PubMed: 29893445]

(5). Betz A, Okamoto M, Benseler F, and Brose N (1997) Direct interaction of the rat unc-13 homologue Munc13−1 with the N terminus of syntaxin. J. Biol. Chem 272, 2520–2526. [PubMed: 8999968]

(6). Sassa T, Harada S, Ogawa H, Rand JB, Maruyama IN, and Hosono R (1999) Regulation of the UNC-18-Caenorhabditis elegans syntaxin complex by UNC-13. J. Neurosci 19, 4772–4777. [PubMed: 10366611]

(7). Brose N, Rosenmund C, and Rettig J (2000) Regulation of transmitter release by Unc-13 and its homologues. Curr. Opin. Neurobiol 10, 303–311. [PubMed: 10851170]

(8). Rosenmund C, Sigler A, Augustin I, Reim K, Brose N, and Rhee JS (2002) Differential control of vesicle priming and short-term plasticity by Munc13 isoforms. Neuron 33, 411–424. [PubMed: 11832228]

(9). Lipstein N, Sakaba T, Cooper BH, Lin KH, Strenzke N, Ashery U, Rhee JS, Taschenberger H, Neher E, and Brose N (2013) Dynamic control of synaptic vesicle replenishment and short-term plasticity by Ca(2+)-calmodulin-Munc13−1 signaling. Neuron 79, 82–96. [PubMed: 23770256]

(10). Lipstein N, Verhoeven-Duif NM, Michelassi FE, Calloway N, van Hasselt PM, Pienkowska K, van Haaften G, van Haelst MM, van Empelen R, Cuppen I, van Teeseling HC, Evelein AM, Vorstman JA, Thoms S, Jahn O, Duran KJ, Monroe GR, Ryan TA, Taschenberger H, Dittman JS, Rhee JS, Visser G, Jans JJ, and Brose N (2017) Synaptic UNC13A protein variant causes increased neurotransmission and dyskinetic movement disorder. J. Clin. Invest 127, 1005–1018. [PubMed: 28192369]

(11). Kapfhamer D, Bettinger JC, Davies AG, Eastman CL, Smail EA, Heberlein U, and McIntire SL (2008) Loss of RAB-3/A in Caenorhabditis elegans and the mouse affects behavioral response to ethanol. Genes, Brain Behav 7, 669–676. [PubMed: 18397381]

(12). Giovedi S, Darchen F, Valtorta F, Greengard P, and Benfenati F (2004) Synapsin is a novel Rab3 effector protein on small synaptic vesicles. II. Functional effects of the Rab3A-synapsin I interaction. J. Biol. Chem 279, 43769–43779. [PubMed: 15265868]

(13). Cosen-Binker LI, Lam PP, Binker MG, Reeve J, Pandol S, and Gaisano HY (2007) Alcohol/cholecystokinin-evoked pancreatic acinar basolateral exocytosis is mediated by protein kinase C alpha phosphorylation of Munc18c. J. Biol. Chem 282, 13047–13058. [PubMed: 17324928]

(14). Yang Y, and Calakos N (2011) Munc13−1 is required for presynaptic long-term potentiation. J. Neurosci 31, 12053–12057. [PubMed: 21849565]

(15). Chen Z, Cooper B, Kalla S, Varoqueaux F, and Young SM Jr. (2013) The Munc13 proteins differentially regulate readily releasable pool dynamics and calcium-dependent recovery at a central synapse. J. Neurosci 33, 8336–8351. [PubMed: 23658173]

(16). Varoqueaux F, Sigler A, Rhee JS, Brose N, Enk C, Reim K, and Rosenmund C (2002) Total arrest of spontaneous and evoked synaptic transmission but normal synaptogenesis in the absence of Munc13-mediated vesicle priming. Proc. Natl. Acad. Sci. U. S. A 99, 9037–9042. [PubMed: 12070347]

(17). Aravamudan B, Fergestad T, Davis WS, Rodesch CK, and Broadie K (1999) Drosophila UNC-13 is essential for synaptic transmission. Nat. Neurosci 2, 965–971. [PubMed: 10526334]

(18). Richmond JE, Davis WS, and Jorgensen EM (1999) UNC-13 is required for synaptic vesicle fusion in C. elegans. Nat. Neurosci 2, 959–964. [PubMed: 10526333]

(19). Ikin AF, Causevic M, Pedrini S, Benson LS, Buxbaum JD, Suzuki T, Lovestone S, Higashiyama S, Mustelin T, Burgoyne RD, and Gandy S (2007) Evidence against roles for phorbol binding protein Munc13−1, ADAM adaptor Eve-1, or vesicle trafficking phosphoproteins Munc18 or NSF as phospho-state-sensitive modulators of phorbol/PKC-activated Alzheimer APP ectodomain shedding. Mol. Neurodegener 2, 23. [PubMed: 18067682]

(20). Nonet ML, Staunton JE, Kilgard MP, Fergestad T, Hartwieg E, Horvitz HR, Jorgensen EM, and Meyer BJ (1997) Caenorhabditis elegans rab-3 mutant synapses exhibit impaired function and are partially depleted of vesicles. J. Neurosci 17, 8061–8073. [PubMed: 9334382]

(21). Bosco DA, and Landers JE (2010) Genetic determinants of amyotrophic lateral sclerosis as therapeutic targets. CNS Neurol. Disord.: Drug Targets 9, 779–790. [PubMed: 20942785]

(22). Su XW, Broach JR, Connor JR, Gerhard GS, and Simmons Z (2014) Genetic heterogeneity of amyotrophic lateral sclerosis: implications for clinical practice and research. Muscle Nerve 49, 786–803. [PubMed: 24488689]

(23). Finsterer J, and Burgunder JM (2014) Recent progress in the genetics of motor neuron disease. Eur. J. Med. Genet 57, 103–112. [PubMed: 24503148]

(24). Diekstra FP, Van Deerlin VM, van Swieten JC, Al-Chalabi A, Ludolph AC, Weishaupt JH, Hardiman O, Landers JE, Brown RH Jr., van Es MA, Pasterkamp RJ, Koppers M, Andersen PM, Estrada K, Rivadeneira F, Hofman A, Uitterlinden AG, van Damme P, Melki J, Meininger V, Shatunov A, Shaw CE, Leigh PN, Shaw PJ, Morrison KE, Fogh I, Chio A, Traynor BJ, Czell D, Weber M, Heutink P, de Bakker PI, Silani V, Robberecht W, van den Berg LH, and Veldink JH (2014) C9orf72 and UNC13A are shared risk loci for amyotrophic lateral sclerosis and frontotemporal dementia: a genome-wide meta-analysis. Ann. Neurol 76, 120–133. [PubMed: 24931836]

(25). Diekstra FP, van Vught PW, van Rheenen W, Koppers M, Pasterkamp RJ, van Es MA, Schelhaas HJ, de Visser M, Robberecht W, Van Damme P, Andersen PM, van den Berg LH, and Veldink JH (2012) UNC13A is a modifier of survival in amyotrophic lateral sclerosis. Neurobiol. Aging 33, 630.e3–630.e8.

(26). Veriepe J, Fossouo L, and Parker JA (2015) Neuro-degeneration in C. elegans models of ALS requires TIR-1/Sarm1 immune pathway activation in neurons. Nat. Commun 6, 7319. [PubMed: 26059317]

(27). Kwan EP, Xie L, Sheu L, Nolan CJ, Prentki M, Betz A, Brose N, and Gaisano HY (2006) Munc13−1 deficiency reduces insulin secretion and causes abnormal glucose tolerance. Diabetes 55, 1421–1429. [PubMed: 16644700]

(28). Das J, Xu S, Pany S, Guillory A, Shah V, and Roman GW (2013) The pre-synaptic Munc13−1 binds alcohol and modulates alcohol self-administration in Drosophila. J. Neurochem 126, 715–726. [PubMed: 23692447]

(29). You Y, and Das J (2020) Effect of ethanol on Munc13−1 C1 in membrane: A Molecular Dynamics Simulation Study. Alcohol.: Clin. Exp. Res 44, 1344–1355. [PubMed: 32424866]

(30). Xu S, Pany S, Benny K, Tarique K, Al-Hatem O, Gajewski K, Leasure JL, Das J, and Roman G (2018) Ethanol regulates presynaptic activity and sedation through presynaptic Unc13 proteins in Drosophila. eNeuro 5, ENEURO.0125-18.2018.

(31). Ma C, Li W, Xu Y, and Rizo J (2011) Munc13 mediates the transition from the closed syntaxin-Munc18 complex to the SNARE complex. Nat. Struct. Mol. Biol 18, 542–549. [PubMed: 21499244]

(32). Betz A, Thakur P, Junge HJ, Ashery U, Rhee JS, Scheuss V, Rosenmund C, Rettig J, and Brose N (2001) Functional interaction of the active zone proteins Munc13−1 and RIM1 in synaptic vesicle priming. Neuron 30, 183–196. [PubMed: 11343654]

(33). Dulubova I, Lou X, Lu J, Huryeva I, Alam A, Schneggenburger R, Sudhof TC, and Rizo J (2005) A Munc13/RIM/Rab3 tripartite complex: from priming to plasticity? EMBO J 24, 2839–2850. [PubMed: 16052212]

(34). Lu J, Machius M, Dulubova I, Dai H, Sudhof TC, Tomchick DR, and Rizo J (2006) Structural basis for a Munc13−1 homodimer to Munc13−1/RIM heterodimer switch. PLoS Biol 4, No. e192. [PubMed: 16732694]

(35). Deng L, Kaeser PS, Xu W, and Sudhof TC (2011) RIM proteins activate vesicle priming by reversing autoinhibitory homodimerization of Munc13. Neuron 69, 317–331. [PubMed: 21262469]

(36). Rizo J, and Südhof TC (2012) The membrane fusion enigma: SNAREs, Sec1/Munc18 proteins, and their accomplices—guilty as charged? Annu. Rev. Cell Dev. Biol 28, 279–308. [PubMed: 23057743]

(37). Shin O-H, Lu J, Rhee J-S, Tomchick DR, Pang ZP, Wojcik SM, Camacho-Perez M, Brose N, Machius M, Rizo J, et al. (2010) Munc13 C 2 B domain is an activity-dependent Ca 2+ regulator of synaptic exocytosis. Nat. Struct. Mol. Biol 17, 280. [PubMed: 20154707]

(38). Basu J, Betz A, Brose N, and Rosenmund C (2007) Munc13−1 C1 domain activation lowers the energy barrier for synaptic vesicle fusion. J. Neurosci 27, 1200–1210. [PubMed: 17267576]

(39). Rhee JS, Betz A, Pyott S, Reim K, Varoqueaux F, Augustin I, Hesse D, Sudhof TC, Takahashi M, Rosenmund C, and Brose N (2002) Beta phorbol ester- and diacylglycerol-induced augmentation of transmitter release is mediated by Munc13s and not by PKCs. Cell 108, 121–133. [PubMed: 11792326]

(40). Kazanietz MG, Lewin NE, Bruns JD, and Blumberg PM (1995) Characterization of the cysteine-rich region of the Caenorhabditis elegans protein Unc-13 as a high affinity phorbol ester receptor. Analysis of ligand-binding interactions, lipid cofactor requirements, and inhibitor sensitivity. J. Biol. Chem 270, 10777–10783. [PubMed: 7537738]

(41). Basu J, Shen N, Dulubova I, Lu J, Guan R, Guryev O, Grishin NV, Rosenmund C, and Rizo J (2005) A minimal domain responsible for Munc13 activity. Nat. Struct. Mol. Biol 12, 1017–1018. [PubMed: 16228007]

(42). Pei J, Ma C, Rizo J, and Grishin NV (2009) Remote homology between Munc13 MUN domain and vesicle tethering complexes. J. Mol. Biol 391, 509–517. [PubMed: 19563813]

(43). Quade B, Camacho M, Zhao X, Orlando M, Trimbuch T, Xu J, Li W, Nicastro D, Rosenmund C, and Rizo J (2019) Membrane bridging by Munc13−1 is crucial for neurotransmitter release. eLife 8, No. e42806. [PubMed: 30816091]

(44). Junge HJ, Rhee J-S, Jahn O, Varoqueaux F, Spiess J, Waxham MN, Rosenmund C, and Brose N (2004) Calmodulin and Munc13 form a Ca2+ sensor/effector complex that controls short-term synaptic plasticity. Cell 118, 389–401. [PubMed: 15294163]

(45). Zhang G, Kazanietz MG, Blumberg PM, and Hurley JH (1995) Crystal structure of the cys2 activator-binding domain of protein kinase C delta in complex with phorbol ester. Cell 81, 917–924. [PubMed: 7781068]

(46). Shen N, Guryev O, and Rizo J (2005) Intramolecular occlusion of the diacylglycerol-binding site in the C1 domain of munc13−1. Biochemistry 44, 1089–1096. [PubMed: 15667202]

(47). Das J, Kedei N, Kelsey JS, You Y, Pany S, Mitchell GA, Lewin NE, and Blumberg PM (2018) Critical Role of Trp-588 of Presynaptic Munc13−1 for Ligand Binding and Membrane Translocation. Biochemistry 57, 732–741. [PubMed: 29244485]

(48). Stewart MD, Cole TR, and Igumenova TI (2014) Interfacial partitioning of a loop hinge residue contributes to diacylglycerol affinity of conserved region 1 domains. J. Biol. Chem 289, 27653–27664. [PubMed: 25124034]

(49). Dries DR, Gallegos LL, and Newton AC (2007) A single residue in the C1 domain sensitizes novel protein kinase C isoforms to cellular diacylglycerol production. J. Biol. Chem 282, 826–830. [PubMed: 17071619]

(50). Das J, and Rahman GM (2014) C1 domains: structure and ligand-binding properties. Chem. Rev 114, 12108–12131. [PubMed: 25375355]

(51). Rahman GM, Shanker S, Lewin NE, Kedei N, Hill CS, Prasad BV, Blumberg PM, and Das J (2013) Identification of the activator-binding residues in the second cysteine-rich regulatory domain of protein kinase Ctheta (PKCtheta). Biochem. J 451, 33–44. [PubMed: 23289588]

(52). Pany S, You Y, and Das J (2016) Curcumin Inhibits Protein Kinase Cα Activity by Binding to Its C1 Domain. Biochemistry 55, 6327–6336. [PubMed: 27776404]

(53). Pany S, Ghosh A, You Y, Nguyen N, and Das J (2017) Resveratrol inhibits phorbol ester-induced membrane translocation of presynaptic Munc13−1. Biochim. Biophys. Acta, Gen. Subj 1861, 2640–2651. [PubMed: 28713022]

(54). Marley J, Lu M, and Bracken C (2001) A method for efficient isotopic labeling of recombinant proteins. J. Biomol. NMR 20, 71–75. [PubMed: 11430757]

(55). Delaglio F, Grzesiek S, Vuister GW, Zhu G, Pfeifer J, and Bax A (1995) NMRPipe: a multidimensional spectral processing system based on UNIX pipes. J. Biomol. NMR 6, 277–293. [PubMed: 8520220]

(56). Williamson MP (2013) Using chemical shift perturbation to characterise ligand binding. Prog. Nucl. Magn. Reson. Spectrosc 73, 1–16. [PubMed: 23962882]

(57). Xu J, Camacho M, Xu Y, Esser V, Liu X, Trimbuch T, Pan Y-Z, Ma C, Tomchick DR, Rosenmund C, and Rizo J (2017) Mechanistic insights into neurotransmitter release and presynaptic plasticity from the crystal structure of Munc13−1 C1C2BMUN. eLife 6, No. e22567. [PubMed: 28177287]

(58). Pany S, Ghosh A, You Y, Nguyen N, and Das J (2017) Resveratrol inhibits phorbol ester-induced membrane translocation of presynaptic Munc13−1. Biochim. Biophys. Acta, Gen. Subj 1861, 2640–2651. [PubMed: 28713022]

(59). Blanco FA, Czikora A, Kedei N, You Y, Mitchell GA, Pany S, Ghosh A, Blumberg PM, and Das J (2019) Munc13 Is a Molecular Target of Bryostatin 1. Biochemistry 58, 3016–3030. [PubMed: 31243993]

(60). Stewart MD, Morgan B, Massi F, and Igumenova TI (2011) Probing the determinants of diacylglycerol binding affinity in the C1B domain of protein kinase Calpha. J. Mol. Biol 408, 949–970. [PubMed: 21419781]

(61). Michelassi F, Liu H, Hu Z, and Dittman JS (2017) A C1-C2Module in Munc13 Inhibits Calcium-Dependent Neurotransmitter Release. Neuron 95, 577–590.e575. [PubMed: 28772122]

(62). Kazanietz MG, Wang S, Milne GW, Lewin NE, Liu HL, and Blumberg PM (1995) Residues in the second cysteine-rich region of protein kinase C δ relevant to phorbol ester binding as revealed by site-directed mutagenesis. J. Biol. Chem 270, 21852–21859. [PubMed: 7665608]

(63). Wang QJ, Fang TW, Nacro K, Marquez VE, Wang S, and Blumberg PM (2001) Role of hydrophobic residues in the C1b domain of protein kinase C delta on ligand and phospholipid interactions. J. Biol. Chem 276, 19580–19587. [PubMed: 11278612]

(64). Giorgione JR, Lin JH, McCammon JA, and Newton AC (2006) Increased membrane affinity of the C1 domain of protein kinase Cdelta compensates for the lack of involvement of its C2 domain in membrane recruitment. J. Biol. Chem 281, 1660–1669. [PubMed: 16293612]

(65). Betz A, Ashery U, Rickmann M, Augustin I, Neher E, Südhof TC, Rettig J, and Brose N (1998) Munc13−1 is a presynaptic phorbol ester receptor that enhances neurotransmitter release. Neuron 21, 123–136. [PubMed: 9697857]

(66). Lipstein N, Verhoeven-Duif NM, Michelassi FE, Calloway N, van Hasselt PM, Pienkowska K, van Haaften G, van Haelst MM, van Empelen R, Cuppen I, van Teeseling HC, Evelein AM, Vorstman JA, Thoms S, Jahn O, Duran KJ, Monroe GR, Ryan TA, Taschenberger H, Dittman JS, Rhee JS, Visser G, Jans JJ, and Brose N (2017) Synaptic UNC13A protein variant causes increased neurotransmission and dyskinetic movement disorder. J. Clin. Invest 127, 1005–1018. [PubMed: 28192369]

(67). Roßner S (2004) New players in old amyloid precursor protein-processing pathways. Int. J. Dev. Neurosci 22, 467–474. [PubMed: 15465276]

(68). de Jesus AJ, and Allen TW (2013) The role of tryptophan side chains in membrane protein anchoring and hydrophobic mismatch. Biochim. Biophys. Acta, Biomembr 1828, 864–876.

(69). Makwana KM, and Mahalakshmi R (2015) Implications of aromatic-aromatic interactions: From protein structures to peptide models. Protein Sci 24, 1920–1933. [PubMed: 26402741]

(70). Grantham R (1974) Amino acid difference formula to help explain protein evolution. Science 185, 862–864. [PubMed: 4843792]

(71). Hristova K, and Wimley WC (2011) A look at arginine in membranes. J. Membr. Biol 239, 49–56. [PubMed: 21107547]

(72). MacCallum JL, Bennett W, and Tieleman DP (2007) Partitioning of amino acid side chains into lipid bilayers: results from computer simulations and comparison to experiment. J. Gen. Physiol 129, 371–377. [PubMed: 17438118]

(73). Rahman GM, and Das J (2015) Modeling studies on the structural determinants for the DAG/phorbol ester binding to C1 domain. J. Biomol. Struct. Dyn 33, 219–232. [PubMed: 24666138]

(74). Kyte J, and Doolittle RF (1982) A simple method for displaying the hydropathic character of a protein. J. Mol. Biol 157, 105–132. [PubMed: 7108955]

(75). Stewart MD, and Igumenova TI (2017) Toggling of Diacylglycerol Affinity Correlates with Conformational Plasticity in C1 Domains. Biochemistry 56, 2637–2640. [PubMed: 28505428]

(76). Liu X, Seven AB, Camacho M, Esser V, Xu J, Trimbuch T, Quade B, Su L, Ma C, Rosenmund C, and Rizo J (2016) Functional synergy between the Munc13 C-terminal C1 and C2 domains. eLife 5, No. e13696. [PubMed: 27213521]

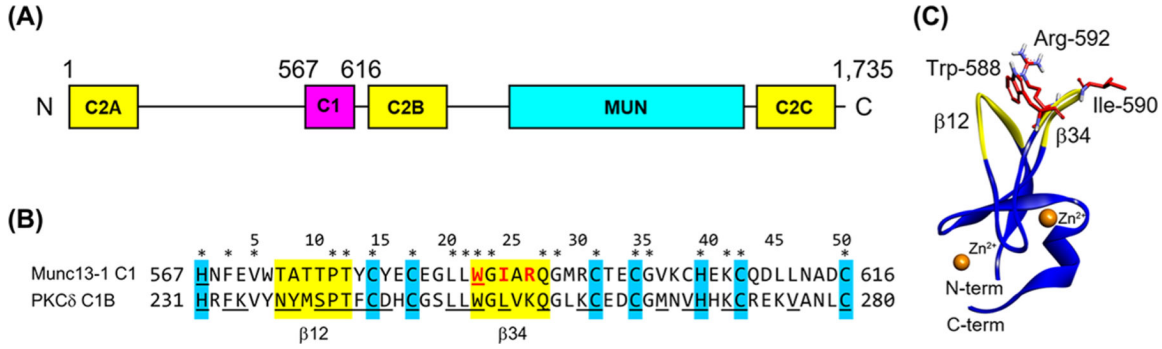

Figure 1.

Domain structure of Munc13-1 and the primary structure of the C1 domain. (A) Domain structure of Munc13-1. The C1 domain binds DAG/phorbol ester, and the C2B domain binds Ca^{2+}. The C1 and C2B domains also bind the lipid membrane. The MUN domain is a self-folding domain consisting of two Munc13 homology domains. (B) Primary sequence of the *Rattus norvegicus* Munc13-1 C1 and PKCδ C1B domains. β12 and β34 loops and Zn^{2+}-coordinating residues are highlighted in yellow and blue, respectively. The asterisks indicate the conserved residues between Munc13-1 C1 and PKCδ C1B. The three residues that are taken up for mutation in this study are colored red. The underlined residues were mutated in previous studies. (C) NMR structure of Munc13-1 C1 (PDB entry 1Y8F). β12 and β34 loops and Zn ions are colored yellow and orange, respectively. The red stick indicates the three residues mutated in this study. N-term and C-term indicate the N- and C-termini, respectively.

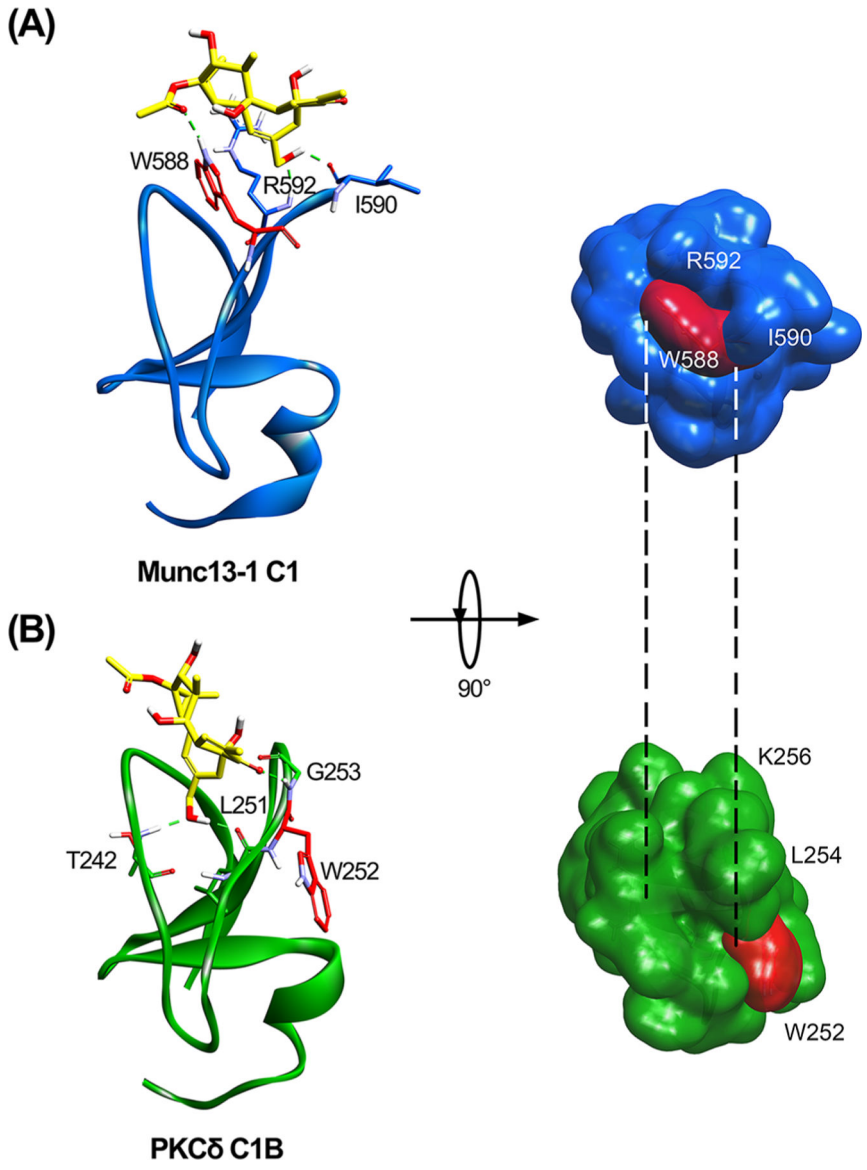

Figure 2.

Ligand binding site of Munc13-1 C1 and PKCδ C1B. (A) Docking of phorbol 13-acetate into the Munc13-1 C1 domain (PDB entry 1Y8F) and the active site of the Munc13-1 C1 domain. The phorbol ester in Munc13-1 interacts with Trp-588, Ile-590, and Arg-592. (B) Phorbol 13-acetate-bound PKCδ C1B (PDB entry 1PTR) and the active site of PKCδ C1B. The phorbol ester in PKCδ interacts with Thr-242, Leu-251, and Gly-253. The line structure represents phorbol 13-acetate (yellow). The green dotted line indicates the three hydrogen bonds in Munc13-1 C1 and the three hydrogen bonds in PKCδ C1B. For Munc13-1, Trp-588, Ile-590, and Arg-592 formed a small pocket. PKCδ C1B has Leu-254 and Lys-256 instead of Ile-590 and Lys-592 of Munc13-1. The geometry of the active site pockets is shown as the top view of the proteins.

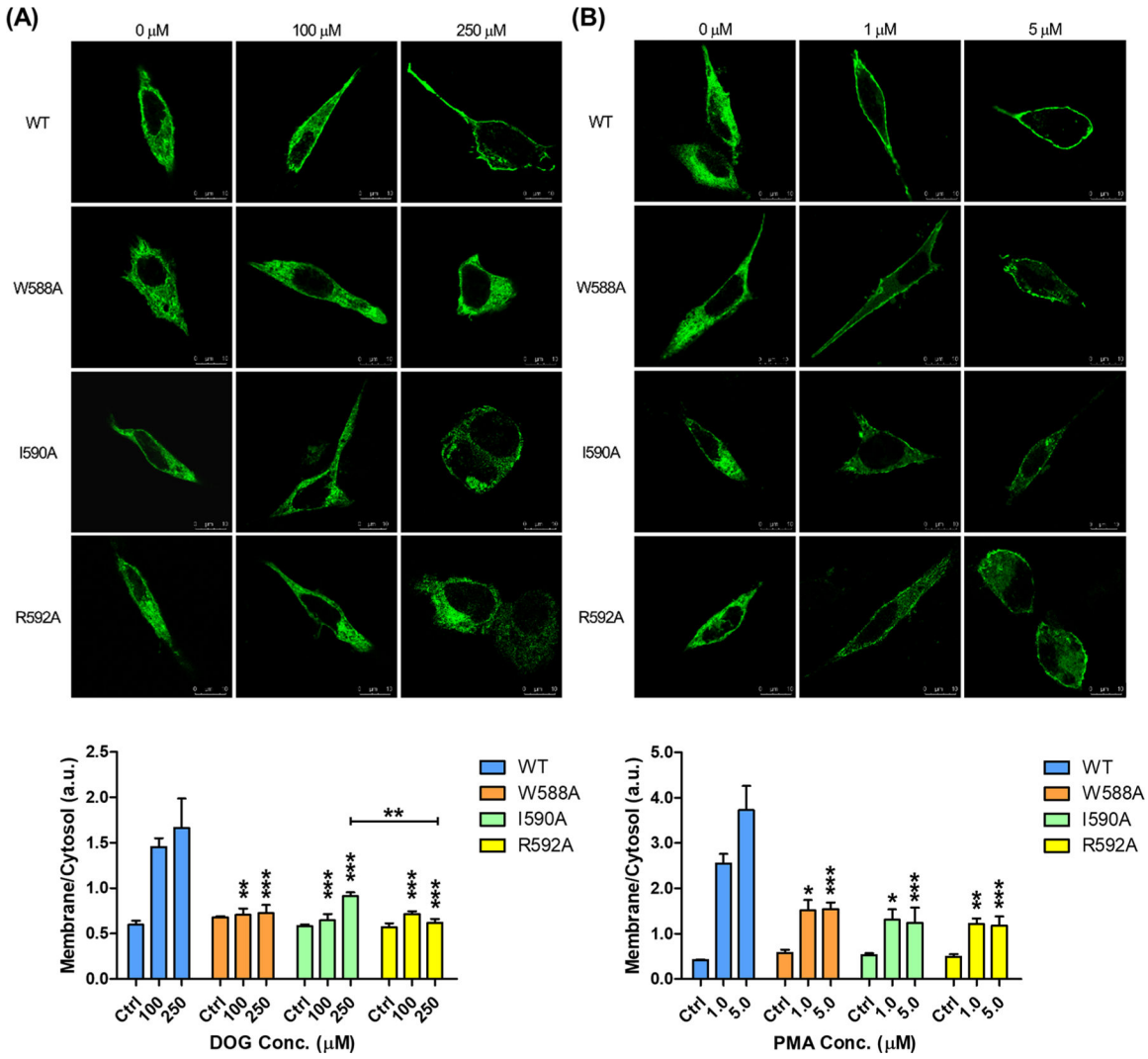

Figure 3.

Translocation of full-length Munc13-1 WT and its mutants after DOG and PMA treatment in HT22 cells. HT22 cells were transfected with GFP-conjugated full-length Munc13-1 WT and its mutants 24 h after plating. Twenty-four hours after transfection with varying concentrations of DOG or PMA and imaging by confocal microscopy, representative confocal images (top) show the distribution of GFP-conjugated Munc13-1 in a cell and the bar graph (bottom) shows the fluorescence intensity ratio of the membrane to the cytosol, quantified from confocal images from multiple experiments. (A) DOG (100 and 250 μM) was used to treat HT22 cells for 15 min. (B) PMA (1.0 and 5.0 μM) was used to treat HT22 cells for 5 min. Quantification data are expressed as means ± the standard error of the mean (SEM) of at least three individual cells. Two-way ANOVA, followed by Bonferroni's post hoc test, was used for analysis of statistical significance. $*P < 0.05$, $**P < 0.01$, and $***P < 0.001$ compared to the WT. Statistical significance was calculated again excluding WT. The significance bar shows the statistical significance among mutants. Ctrl, control group. Confocal analysis was performed as described in Materials and Methods.

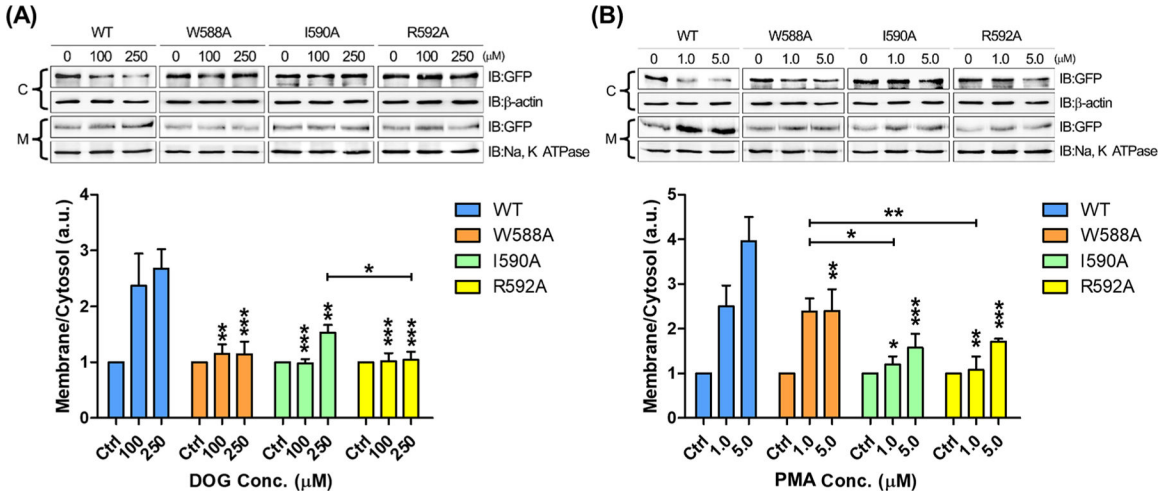

Figure 4.

Effect of the single mutation in three residues on Munc13-1 membrane translocation. HT22 cells were transfected with GFP-conjugated full-length Munc13-1 WT and its mutants 24 h after plating. Twenty-four hours after transfection, varying concentrations of DOG or PMA were applied and cells were fractionated to cytosolic and membrane fractions. Representative Western blot analysis (top) shows the cytosolic fraction (C) and membrane fractions (M) of the wild type and the three Munc13-1 mutants after DOG or PMA had been administered for 15 or 5 min to HT22 cells, respectively. The bar graph (bottom) shows normalized densitometric analysis of the immunoblots from multiple experiments. (A) DOG (100 and 250 μM) was used to treat HT22 cells for 15 min. (B) PMA (1.0 and 5.0 μM) was used to treat HT22 cells for 5 min. Data are expressed as means ± SEM of three independent experiments. Two-way ANOVA, followed by Bonferroni's multiple-comparison post hoc test, was used for analysis of statistical significance. *$P < 0.05$, **$P < 0.01$, and ***$P < 0.001$ compared to the WT. Statistical significance was calculated again excluding the WT. The significance bar shows the statistical significance among mutants. Ctrl, control group. Cell fractionation and Western blot analysis were performed as described in Materials and Methods.

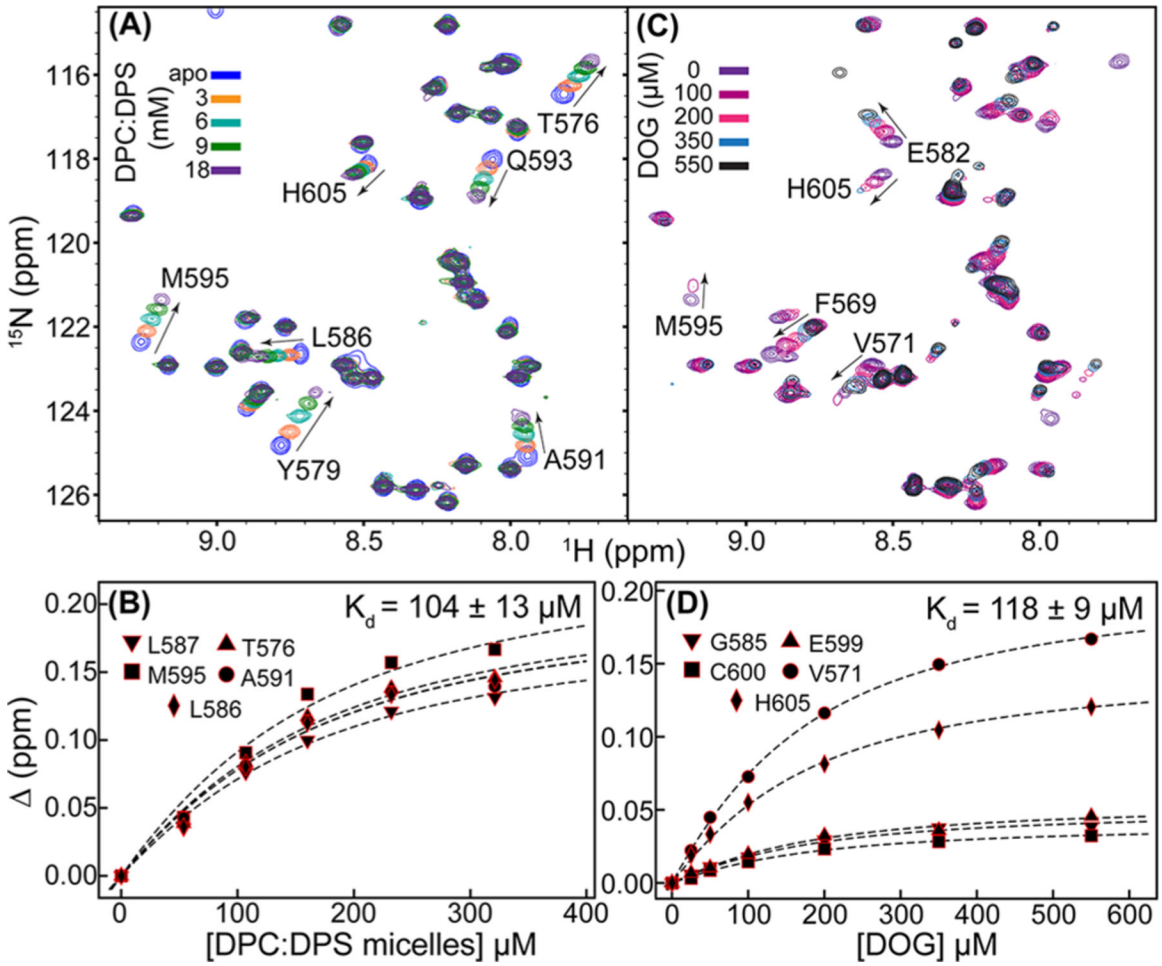

Figure 5.

Partitioning of the Munc13-1 C1 domain into micelles in a ligand-independent manner and its weak binding to diacylglycerol. (A) Spectral expansions and overlays of 100 μM U-^{15}N-enriched Munc13-1 C1 titrated with the DPC/DPS (70:30) mixed micelles. The binding of C1 to micelles is in the fast exchange regime on the NMR chemical shift time scale. (B) Combined chemical shift perturbations (Δ, parts per million) for select residues plotted as a function of detergent concentration. The apparent dissociation constant (K_d) of 104 μM was obtained using the single-site binding model. (C) Spectral expansions and overlays of the diacylglycerol (DOG) titration in the presence of 20 mM DPC/DPS (70:30) mixed micelles. (D) Combined chemical shift perturbations (Δ, parts per million) for select residues plotted as a function of DOG concentration. The apparent K_d of 118 μM was obtained using the single-site binding model.

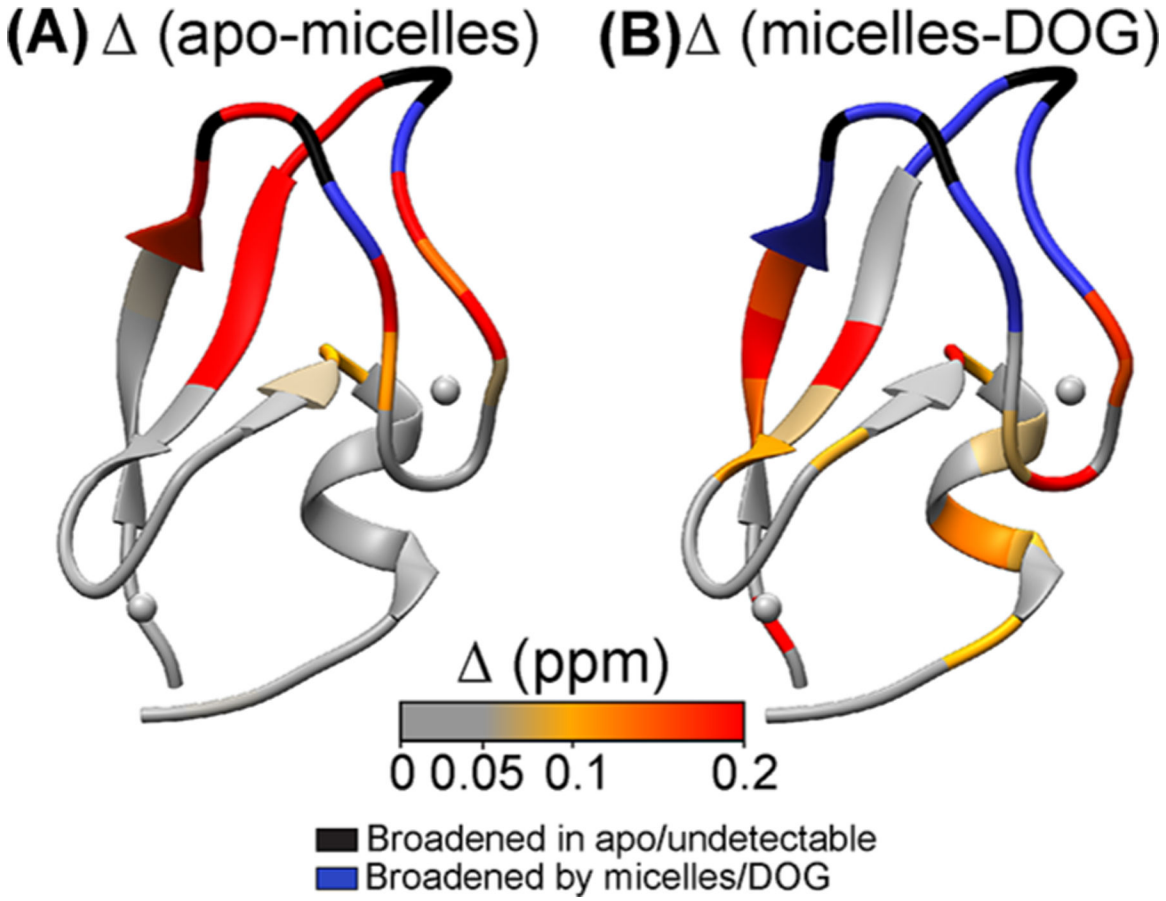

Figure 6.

Loop regions, their hinges, and the α-helical segment are affected by the Mun13-1 C1−diacylglycerol interactions. The CSPs due to binding of (A) micelles and (B) DOG are mapped onto the lowest-energy conformer of the Munc13-1 C1 NMR ensemble (PDB entry 1Y8F). The apo NMR spectrum was used as a reference to calculate perturbations upon addition of 20 mM DPC/DPS (70:30) mixed micelles (A). This micelle spectrum served as the reference to calculate perturbations upon addition of 0.55 mM DOG (B).

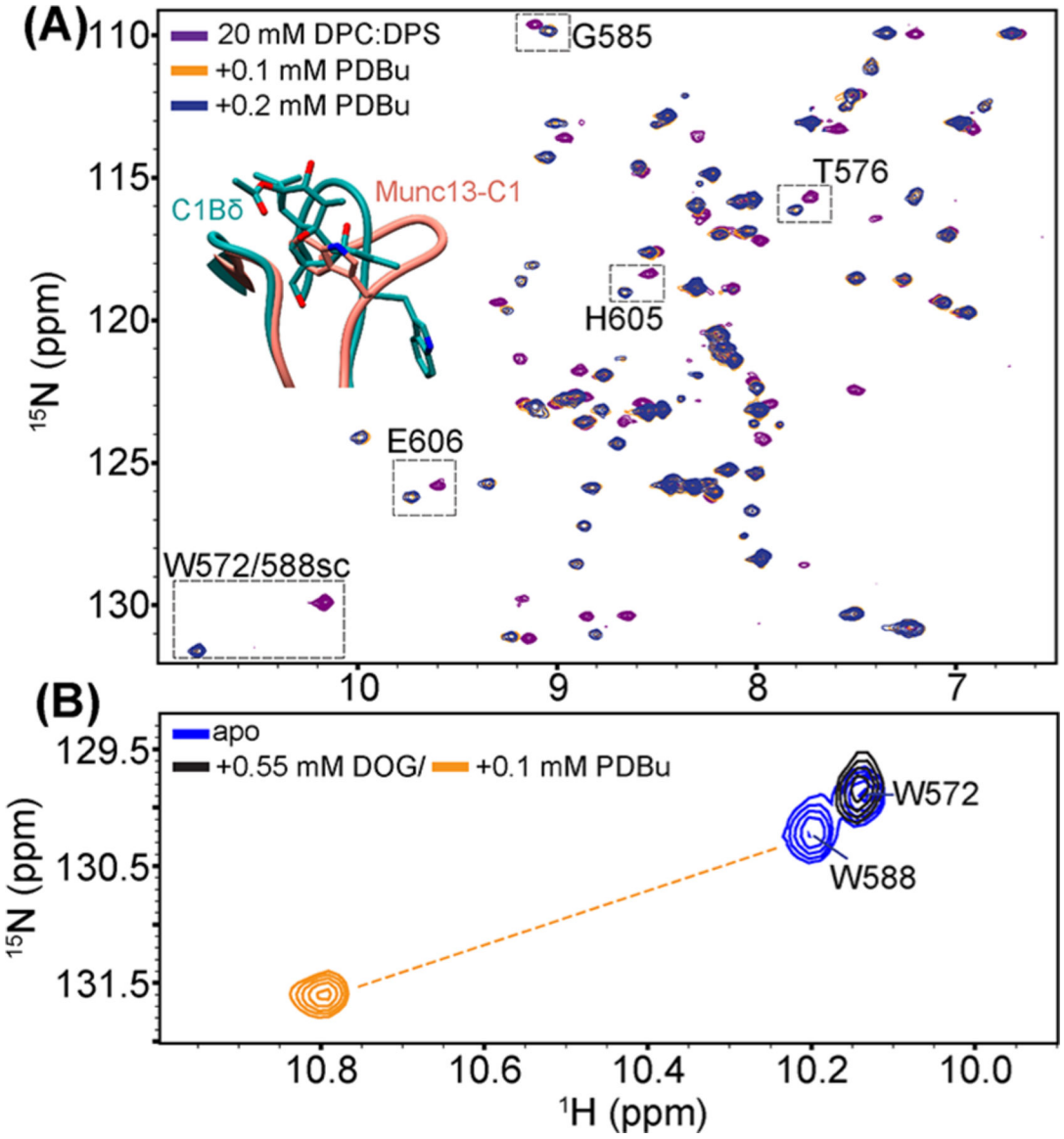

Figure 7.

Munc13-1 C1 domain that forms a complex with PDBu at stoichiometric protein and ligand concentrations. (A) Spectral overlays of 100 μM U-^{15}N-enriched Munc13-1 C1 domain in the presence of 20 mM DPC/DPS (70:30) mixed micelles with 100 and 200 μM PDBu. The residues mentioned in the text are labeled and highlighted by squares. The inset shows the structural overlay of PKCδ C1B bound to phorbol 13-acetate (X-ray, PDB entry 1PTR) and the apo Munc13-1 C1 domain (NMR, PDB entry 1Y8F, lowest-energy conformer) showing the phorbol ester binding site occluded by Trp-588 in Munc13-1 C1. (B) Spectral overlay comparing the Trp side chain (Nε–Hε) perturbations with DOG and PDBu, both in the presence of 20 mM DPC/DPS (70:30) mixed micelles. The downfield-shifted resonance is observed upon addition of PDBu, with the corresponding broadening of both Trp-572 and −588 side chain resonances. With DOG, only the Trp-588 side chain resonance is broadened beyond detection. The drastic shifts of these resonances are consistent with the

conformational change associated with the displacement of Trp-588 from the binding groove by the PDBu (inset of panel A).

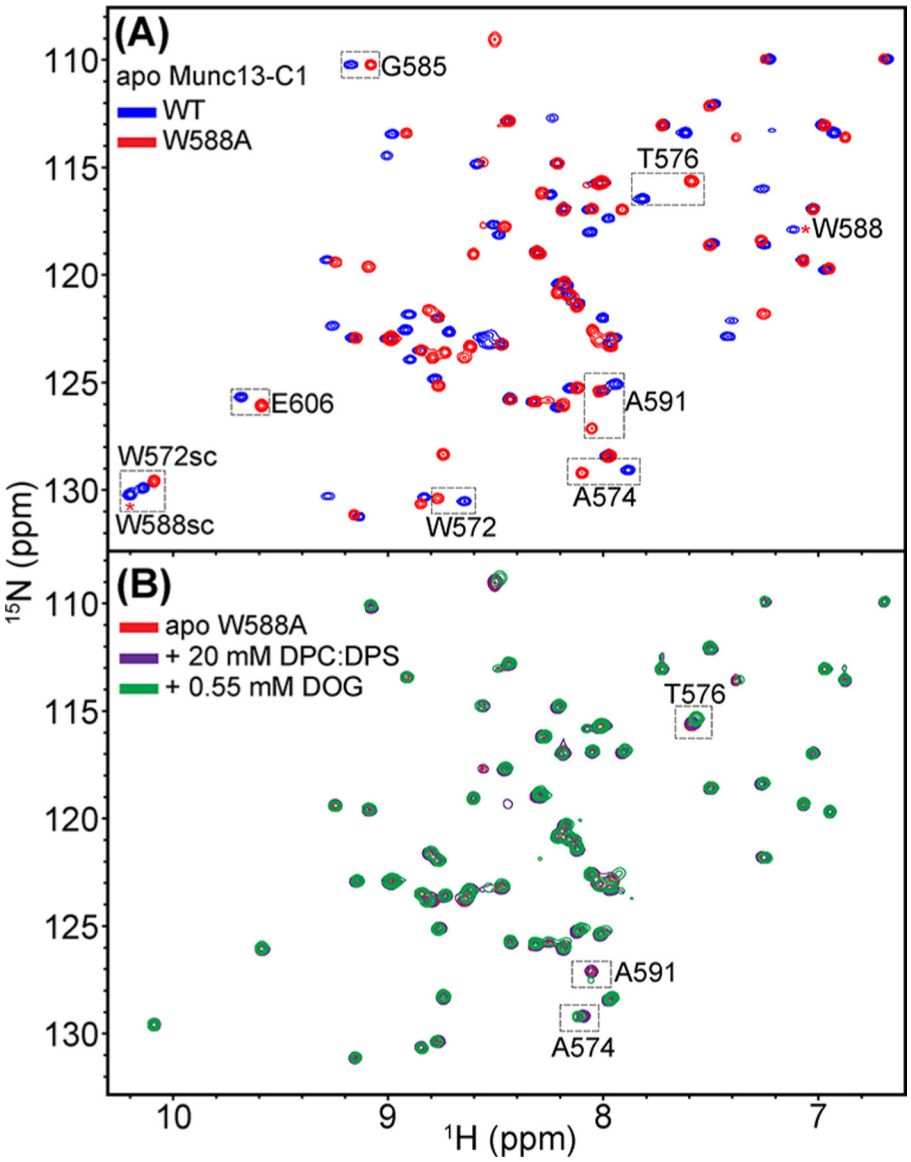

Figure 8.

Trp-588 is essential for the ligand-independent partitioning of the Munc13-1 C1 domain into a hydrophobic environment. (A) Spectral overlay of 100 μM U-^{15}N-enriched WT and W588A Munc13-1 C1 domains. Select perturbed residues are highlighted by squares. (B) Spectral overlay of 100 μM U-^{15}N-enriched W588A Munc13-1 C1 domain in the presence of 20 mM DPC/DPS (70:30) mixed micelles and 0.55 mM DOG. Failure of the W588A variant to partition into micelles precludes its interactions with DOG.

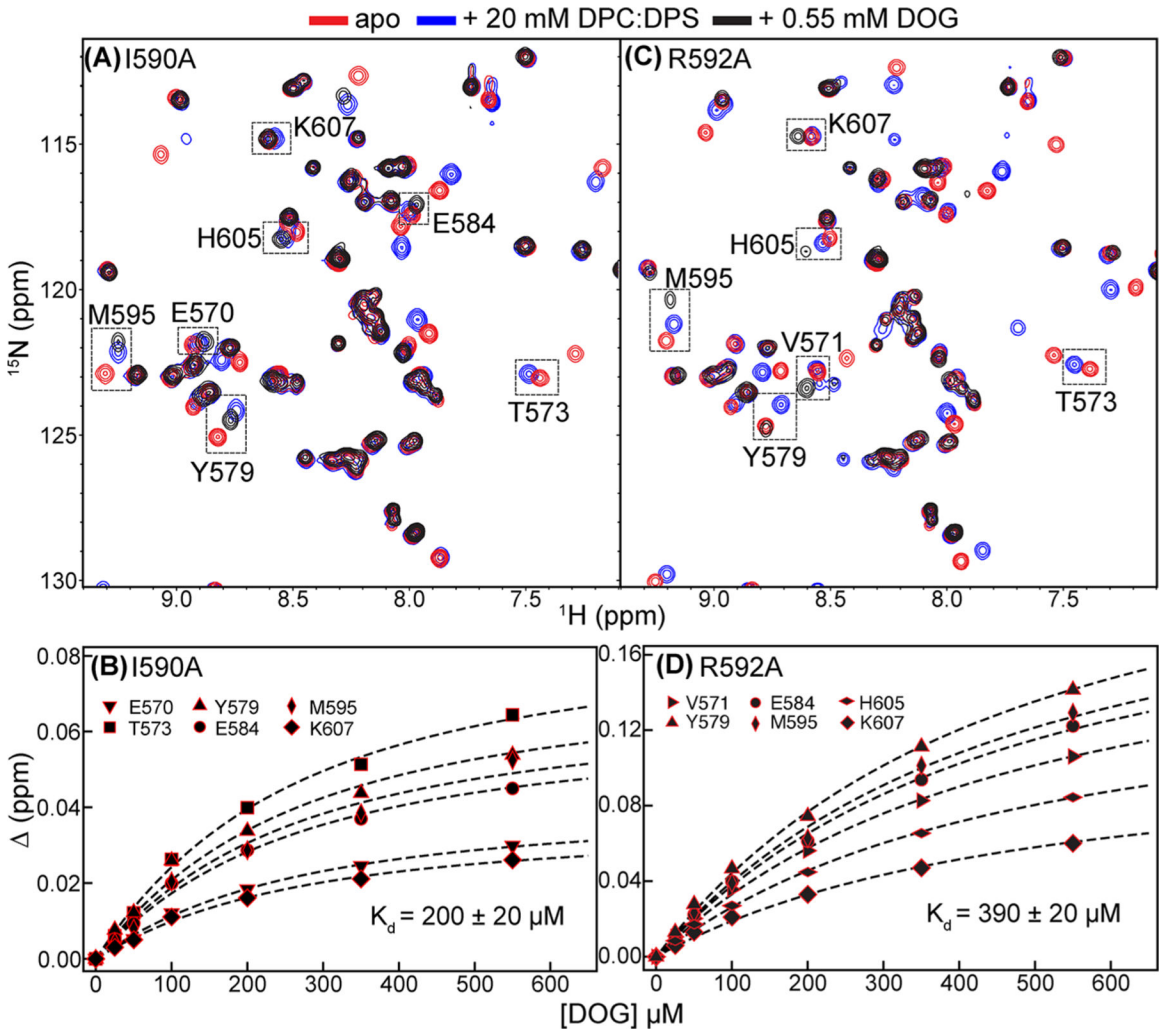

Figure 9.

I590A and R592A bind DOG with affinities 1.5- and 3-fold lower, respectively, than that of WTC1. (A) Spectral overlay of 100 μM U-^{15}N-enriched apo I590A variant, in the presence of 20 mM DPC/DPS (70:30) mixed micelles, and with 0.55 mM DOG. The residues used for quantifying the affinity are highlighted by squares. (B) Combined chemical shift perturbations (Δ, parts per million) for select residues plotted as a function of DOG concentration. An apparent dissociation constant (K_d) of 200 μM was obtained using the single-site binding model. (C) Spectral overlay of 100 μM U-^{15}N-enriched apo R592A variant, in the presence of 20 mM DPC/DPS (70:30) mixed micelles, and with 0.55 mM DOG. The residues used to quantify the affinity are highlighted by squares. (D) Combined chemical shift perturbations (Δ, parts per million) for select residues plotted as a function of DOG concentration. A dissociation constant (K_d) of 390 μM was obtained using the single-site binding model.